THE ASTROPHYSICAL JOURNAL, 490:143–155, 1997 November 20

WHERE DO THE DISKS OF SPIRAL GALAXIES END?

J. BLAND-HAWTHORN
Anglo-Australian Observatory, P.O. Box 296, Epping, NSW 2121, Australia
AND
K. C. FREEMAN AND P. J. QUINN[1]
Mount Stromlo and Siding Springs Observatories, Australian National University, Private Bag, Weston Creek P.O., ACT 2611, Australia
Received 1997 March 6; accepted 1997 June 24

ABSTRACT

In spiral galaxies, the H I surface density declines with increasing radius to a point at which it is seen to truncate dramatically in the best observed cases. If the ambient radiation field is sufficiently strong, there exists a maximum radius beyond which the cold gas is unable to support itself against ionization. We have now succeeded in detecting ionized gas beyond the observed H I disk in spirals. Here we report on our findings for the Sculptor galaxy NGC 253. The H I disks in Sculptor galaxies extend to only about $1.2R_{25}$, although we have detected ionized gas to the limits of our survey, out to $1.4R_{25}$. This has important ramifications for spiral galaxies in that it now becomes possible to trace the gravitational potential beyond where the H I disk ends. The detections confirm that the rotation curve continues to rise in NGC 253, as it appears to do for other Sculptor galaxies, from the H I measurements, but there is a hint that the rotation curve may fall abruptly not far beyond the edge of the H I disk. If this is correct, it suggests that the dark halo of NGC 253 may be truncated near the H I edge and provides further support for the link between dark matter and H I. The line ratios are anomalous with [N II] λ6548 to Hα ratios close to unity. While metallicities at these large radii are uncertain, such enhanced ratios, compared to solar-abundance H II regions ([N II] λ6548/Hα = 0.05–0.2), are likely to require selective heating of the electron population without further ionization of N^+. We discuss the most likely sources of ionization and heating, and the possible role of refractory element depletion (e.g., Ca, Si, and Fe) onto dust grains.

Subject headings: galaxies: ISM — galaxies: kinematics and dynamics — galaxies: spiral — galaxies: structure

1. INTRODUCTION

The case for dark matter in galaxies rests primarily on spiral galaxies in which the H I rotation curve has been measured at radii that are several times larger than the optical disk. At these large radii, the observed rotation of the gas is fully a factor of 2 larger than that expected for circular orbits in the potential field of the luminous galaxy (van Albada et al. 1985). Many of these extensive rotation curves are flat or even rising at the outermost points, which means that the edge of the mass distribution has not yet been found (Puche & Carignan 1991). In an attempt to find the edge, several observers have pushed their H I observations to higher sensitivity (van Gorkom 1993; Corbelli, Schneider, & Salpeter 1989). These observations have shown that H I disks are abruptly truncated at column densities near 10^{19} atoms cm^{-2} where the rotation curves are still flat.

One possible explanation for the truncation is that at large radii, the thin H I disks become fully ionized by the metagalactic UV background (Bochkarev & Sunyaev 1977). If this is the case, the outer parts of gaseous disks should be emitting Hα photons. Maloney (1993) has shown that the expected Hα emission measure from the ionized disk beyond the truncation point falls in the range 0.025–0.25 cm^{-6} pc. After demonstrating that these flux levels are quite feasible with the TAURUS-2 Fabry-Perot interferometer (Bland-Hawthorn et al. 1994, hereafter BTVS), we now use this technique to search for the signature of ionized gas at and beyond the H I edge in Sculptor spirals.

The implications of a positive detection are profound. If the outer disk could be detected, we would know how extensive galactic disks (and dark halos) really are, and we could continue tracking the rotation curve in order to find the edge of the halo and hence the total mass of galaxies. A positive detection also has important implications for explaining low-redshift Lyα absorption-line systems toward quasars and for constraining the poorly known metagalactic ionizing background.

In § 2 we describe the observations carried out at the Anglo-Australian Telescope (AAT). In § 3 we derive the expected level of Hα emission at an H I edge and describe the experimental procedure for achieving such faint detections. The reduction and analysis steps are briefly outlined in § 4, the results of which are discussed in § 5. In § 6 we attempt a physical interpretation of both the gas kinematics and the gas excitation, before drawing our conclusions in § 7.

2. OBSERVATIONS

The observations were carried out over three long, dark nights (1994 August 9–12) at the f/7.91 Cassegrain focus of the AAT 3.9 m. Follow-up observations were carried out at f/14.9 on 1995 September 27. The TAURUS-2 interferometer was used in conjunction with the refurbished HIFI 40 μm gap Queensgate etalon and a four-cavity blocking filter (90% peak transmission), centered at λ6555, with a 45

[1] Current address: European Southern Observatory, Karl-Schwarzschild-Strasse 2, 85748 Garching bei München, Germany.

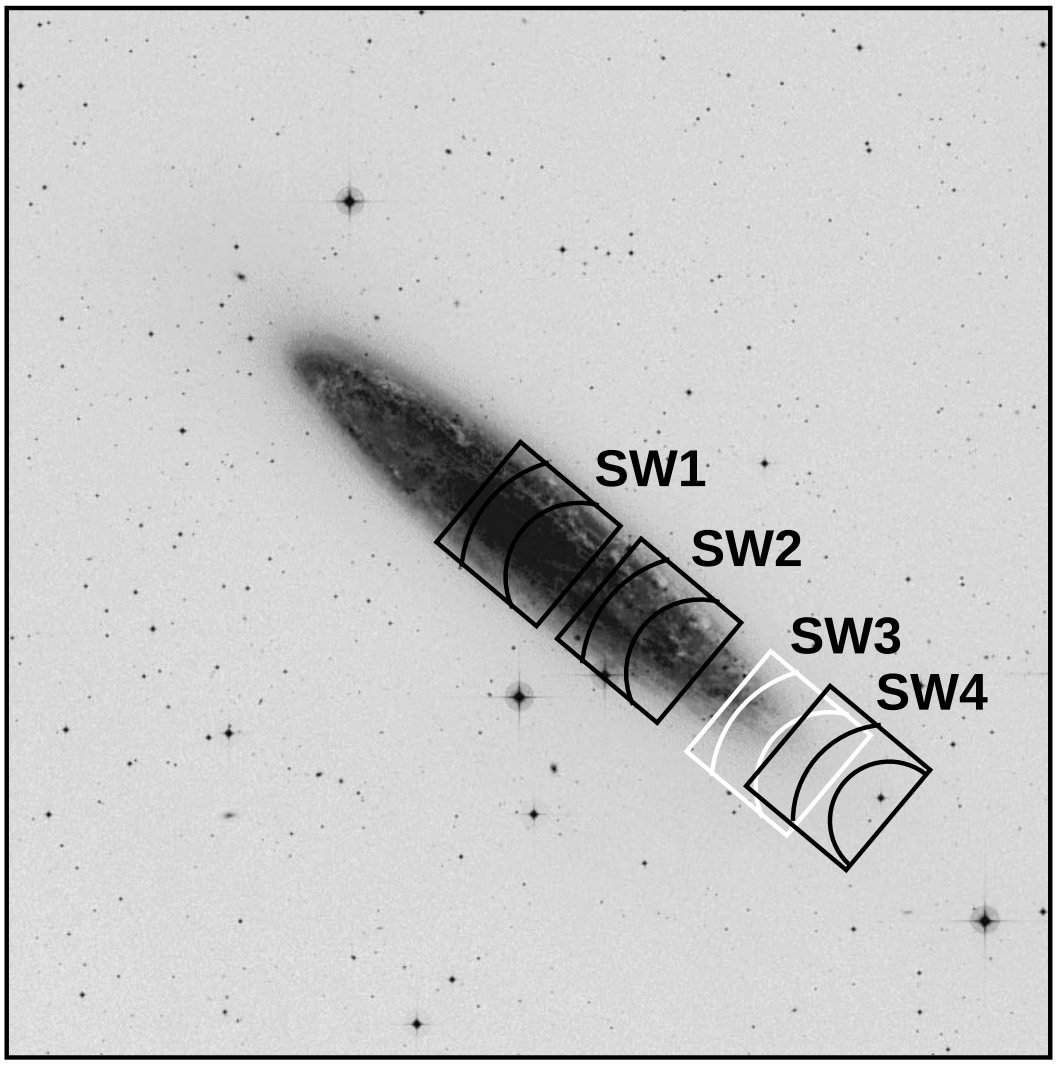

FIG. 1.—TAURUS-2 5′ fields (SW1, SW2, SW3, SW4) superposed on a *B* image of NGC 253. The blue [N II] line occurs at smaller galactic radii, compared to the Hα line in the same field. There are four distinct fields with two emission lines occurring in each. At the central position, the etalon was used at two different spacings, which meant that we obtained line detections at four discrete positions.

Å bandpass well matched to the etalon free spectral range (54.3 Å at Hα). The 50 mm filter was placed out of focus close to the focal plane and baffled to give a 5.0 field. The etalon was tilted by 3.°4 to shift the optical axis to the field edge. An in-focus, focal-plane colander mask was used to ensure that low-order ghosts fall outside the field of view. The TAURUS-2 f/8 pupil diameter is 59.9 mm, which is oversized for the 50 mm diameter etalon. Because of uncertainties of the precise location of the optical cavity within the etalon, we placed a 45.0 mm aperture stop immediately in front of the etalon. The pupil stop introduced a major loss of light (50%), compounded by a Cassegrain hole which is 17% of the total pupil area. The full pupil was used in the f/15 observations. The observational setup was the same, except for a 75 mm blocking filter centered at λ6585 that was not baffled, thereby producing a field of view similar to the f/8 observations.

Observations were made at four positions in NGC 253 (Figs. 1 and 2), with several discrete tunings of the etalon at each position (Table 1). The etalon was used at fixed-gap spacings, and the resulting ring pattern was imaged onto a Tek 1024^2 CCD with pixel scales of 0.″594 pixel^{-1} (f/8) and 0.″315 pixel^{-1} (f/15) with read noise $\approx 2.3e^-$. The wavelength range λλ6550–6590 is dispersed quadratically over the 5′ field at 1 Å resolution, with blue wavelengths to the north. The instrument and detector were rotated to a position angle of 230° in order to align the detector with the galaxy major axis. At both foci, we observed two stellar flux standards (Table 1); at f/8, we also observed four planetary nebulae. Observations were also made of blank fields and in the direction of the Smith high-velocity cloud (Smith 1963; Wakker 1991), and twilight flats were taken on all nights, with and without the etalon.

3. EXPERIMENT

3.1. *The Expected* Hα *Flux*

We now derive the expected flux levels from spiral edges ionized by a metagalactic radiation field. The surface density of H I gas falls exponentially in spiral galaxies. A point is reached at which the H I column is no longer able to support itself against ionization by the cosmic radiation field. A naive calculation can be used to predict the expected column density $N_{\rm H}$ at which this is likely to occur, in addi-

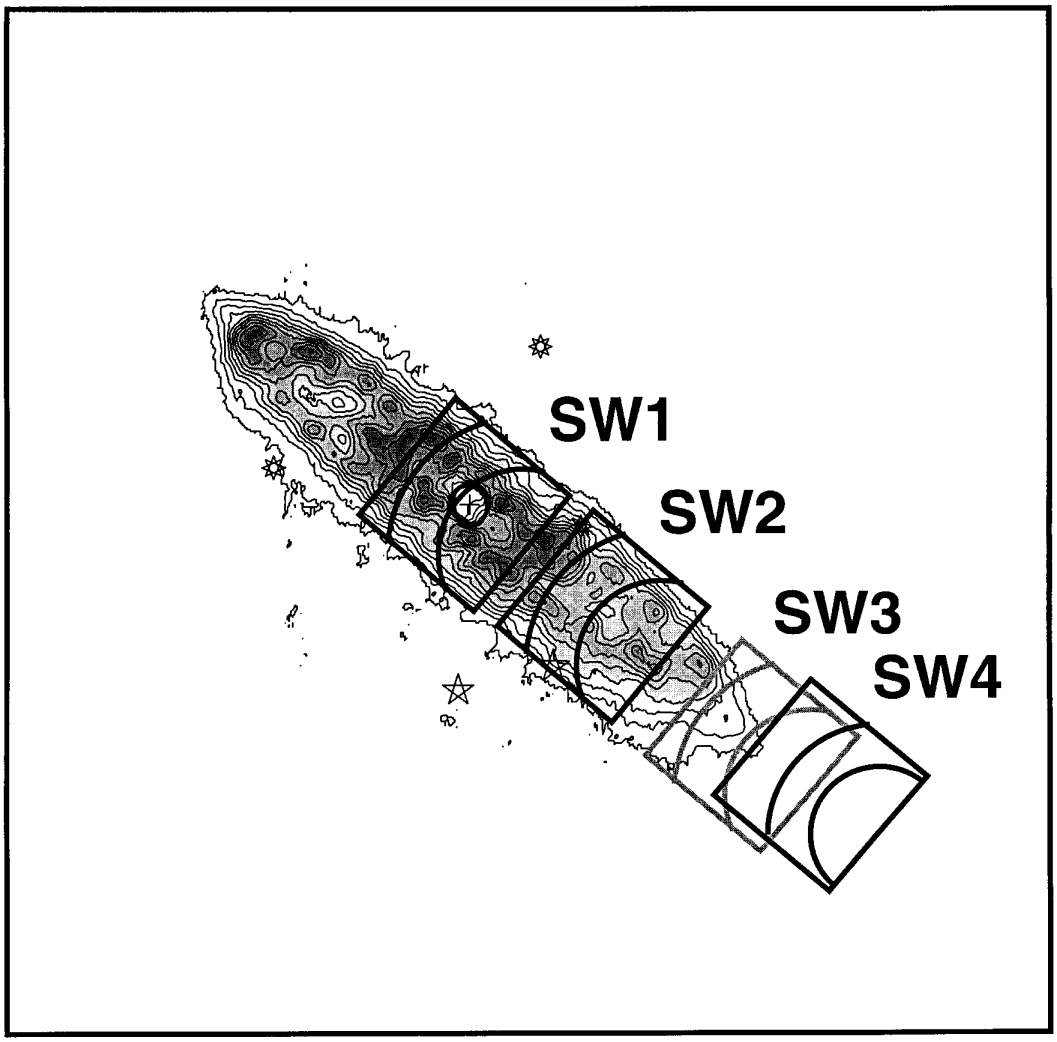

FIG. 2.—Same as Fig. 1, but the TAURUS-2 fields have been superposed onto a deep ATNF H I map (Koribalski, Whiteoak, & Houghton 1995). The outermost H I contour corresponds to a column density of 5×10^{20} cm^{-2}.

tion to the local electron density, n_e, and the expected emission measure, $\mathscr{E}_m$. More sophisticated treatments are given in Maloney (1993) and Dove & Shull (1994).

We shall assume that, at a large galactocentric radius, the ionization rate is in rough equilibrium with the rate of recombination. Therefore, along an axis z, perpendicular to the galactic disk, we find

$$2\alpha_B \int_0^\infty n_e n_p \, dz = \int_{\nu_0}^\infty \frac{4\pi J_\nu}{h\nu} \, d\nu \, , \tag{1}$$

where the recombination coefficient α_B depends on the neutral hydrogen column and on the local electron temperature (case B: $\alpha_B \approx 2 \times 10^{-13}$ cm^3 s^{-1} at $T_e = 10^4$ K). The local electron density n_e (and therefore the proton density n_p) is related to the neutral hydrogen density $n_{\rm H}$ through the ionizing fraction χ, such that $n_e = \chi n_{\rm H}$. Equation (1) assumes that the neutral gas sheet is ionized from both sides. We approximate the cosmic ionizing flux level as

$$J_\nu = 10^{-21} J^0_{-21} \left(\frac{\nu_0}{\nu}\right)^\beta \text{ ergs cm}^{-2} \text{ s}^{-1} \text{ Hz}^{-1} \text{ sr}^{-1} \, , \tag{2}$$

where J^0_{-21} is the metagalactic flux at the Lyman limit ($\nu = \nu_0$) in units of ergs cm^{-2} s^{-1} Hz^{-1} sr^{-1}. If the cosmic ionizing field (e.g., Haardt & Madau 1996) results largely from quasars at high redshift, β is approximately unity.

For an exponential disk with density profile $n_{\rm H} = n^0_{\rm H} \exp(-z/z_s)$, the electron density in the plane of the galaxy at the ionized edge is

$$n^0_{\rm H} \approx 1.8 \chi^{-1} \sqrt{J^0_{-21} (z_s \beta)^{-1}} \text{ cm}^{-3} \, , \tag{3}$$

where the vertical scale height of the disk z_s is in parsecs. We assume a value of $z_s = 100$ pc throughout. The particle column density perpendicular to the disk is

$$N_{\rm H} = 2 \int_0^\infty n_{\rm H} \, dz \tag{4}$$

$$\approx 1.1 \times 10^{19} \chi^{-1} \sqrt{J^0_{-21} z_s \beta^{-1}} \text{ cm}^{-2} \, . \tag{5}$$

For a 2 σ upper limit $J^0_{-21} = 0.08$ ergs cm^{-2} s^{-1} Hz^{-1} sr^{-1} (Vogel et al. 1995; Bland-Hawthorn 1997), the gas is fully ionized when $n^0_{\rm H} \approx 0.05$ cm^{-3} and $N_{\rm H} \approx 3 \times 10^{19}$ cm^{-2}. The latter is in good agreement with observations (e.g., Corbelli et al. 1989). A crude upper limit on the Hα emission measure $\mathscr{E}_m$ is

$$\mathscr{E}_m = \int n_e n_p \, dl \approx 0.25 \text{ cm}^{-6} \text{ pc} \, . \tag{6}$$

TABLE 1

TAURUS-2 OBSERVING LOG

Object (1)	Focus (2)	Exposures (3)	Date (4)	Filter (5)	Gap (6)	Air Mass (7)	Seeing (8)	P.A. (deg) (9)
Flux Standard: Line								
N6072	f/8	6	1994 Aug 9	6555/45/0	...	1.1	1.0	0
N6302	f/8	6	1994 Aug 9	6555/45/0	...	1.1	1.3	0
N6445	f/8	6	1994 Aug 10	6555/45/0	...	1.1	1.3	0
N6563	f/8	6	1994 Aug 10	6555/45/0	...	1.1	1.3	0
Flux Standard: Continuum								
LTT 7379	f/8	3 × 1	1994 Aug 9	6555/45/0	...	1.1	1.7	0
CD-32 9927	f/8	3 × 2	1994 Aug 10	6555/45/0	...	1.1	1.3	0
HZ 7.....	f/15	2	1995 Sep 27	6585/43/8	260	1.4	0.9	230
Hiltner 600.....	f/15	2	1995 Sep 27	6585/43/8	260	1.3	0.9	230
Blank Fields								
Sky 1	f/8	6 × 20	1994 Aug 11	6555/45/0	180	1.3–1.9	1.4	230
Smith 1	f/8	6 × 20	1994 Aug 9	6555/45/0	200	1.4	1.7	0
Smith 2	f/8	8 × 20	1994 Aug 10	6555/45/0	200	1.4	1.3	0
Smith 2	f/8	5 × 20	1994 Aug 11	6555/45/0	180	1.2–1.3	1.3	230
Object Fields								
N253 1 (SW1).....	f/8	5	1994 Aug 10	6555/45/0	200	1.7	1.3	230
N253 2 (SW2).....	f/8	10	1994 Aug 10	6555/45/0	200	1.2	1.3	230
N253 2 (SW2).....	f/8	5	1994 Aug 10	6555/45/0	260	1.2	1.3	230
N253 3 (SW3).....	f/8	18 × 20	1994 Aug 10	6555/45/0	260	1–1.4	1.3	230
N253 4 (SW4).....	f/8	16 × 20	1994 Aug 11	6555/45/0	240	1–1.9	1.5	230
N253 3 (SW3).....	f/15	2 × 20	1995 Sep 27	6585/43/8	260	1.2–1.4	1.0	230
N253 3 (SW3).....	f/15	5 × 30	1995 Sep 27	6585/43/8	260	1.4–1.6	0.9	230

NOTE.—Col. (1): Object name; col. (2): AAT focus; col. (3): exposure times (minutes); col. (4): local date of observation; col. (5): blocking filter/bandwidth (Å)/tilt angle; col. (6): etalon gap in BCV units (ellipsis indicates full FSR scanned); col. (7): average air mass; col. (8): seeing disk FWHM; and col. (9): position angle of detector on the sky.

This surface brightness, equivalent to 90 millirayleighs (mR) and 5×10^{-19} ergs cm^{-2} s^{-1} arcsec^{-2}, is reached at the 3 σ level by the Fabry-Perot "staring" technique in less than 1 hr of observation (BTVS).[2]

3.2. *Fabry-Perot Staring*

We exploit the staring technique in order to obtain a single, extremely deep spectrum of a diffuse source that fills the field of view. For a fixed gap spacing, $\lambda \propto \cos\theta$, where θ is the angle of an incoming ray of wavelength λ to the optical axis. The spectrum in a narrow band ($\sim$40 Å) is dispersed radially from the optical axis across the field (see Fig. 3). As with long-slit spectrometers, the instrumental profile is projected onto the detector, but the line FWHM in pixels varies across the field inversely with θ. Complete Fabry-Perot rings have constant surface brightness and equal spectroscopic resolution. After flat-fielding and point-source removal, the data are binned azimuthally and resampled to a linear axis to obtain a single deep spectrum (e.g., Figs. 4 and 5).

Maximum sensitivity is achieved when (*a*) the detector covers the unvignetted field; (*b*) the line-emitting source fills the field of view; and (*c*) the velocity range and internal kinematic dispersion, taken together, are comparable to the instrumental profile width. These criteria determine which galaxies are best matched to a given instrument.

The isovelocity contours of a disk undergoing flat rotation show two distinct regimes. The central region of solid-body rotation gives rise to contours that are parallel to the kinematic minor axis. At the turnover radius, the contours become radial and therefore subtend a fixed angle, as seen on the sky about the kinematic major axis. The spread in velocity within a fixed field of view declines inversely with radius, until we reach the intrinsic spread of an isothermal H I disk ($\sigma_{\rm H\,I} \approx 10$ km s^{-1}; Kamphuis 1993). An important concept is the angular extent of the innermost monochromatic field (imf) for a given instrument, telescope, and object. We define this as the field at the smallest radius along the disk major axis within which the observed spread in velocities does not exceed the instrumental resolution. The necessary condition for a galaxy with maximum deprojected velocity $v_{\rm max}$, inclined at an angle i, is

$$v_{\rm max}^2(\sin^2 i)\left[1+\left(\frac{\mu F_{\rm kpc}}{2R\sin i}\right)^2\right]^{-1} + \sigma_{\rm H\,I}^2 \le \sigma_{\rm FP}^2 , \qquad (7)$$

where $\sigma_{\rm FP}$ is the instrumental width (in km s^{-1}) and R is the radius to the field center (in kpc). Truncated H I edges typically occur at radii larger than the semimajor axis distance (R_{25} in kpc) of the $B = 25$ mag arcsec^{-2} contour. For a fixed field $F_{\rm kpc}$ (in kpc), this condition is most easily satisfied in large, nearby galaxies where the instrument field of view is a small fraction of the object size. The constant μ allows for two different approaches to sky subtraction. If this is achieved through a separate exposure, $\mu = 1$; otherwise, in a properly matched experiment, we assume that half of the field is given over to the sky background, for which $\mu = 0.5$.

The optimal disk inclination is unclear: face-on galaxies have a smaller velocity spread and subtend larger solid angles, whereas inclined disks have a higher projected column density. A potential problem in edge-on disks is

[2] 1 rayleigh = $10^6/4\pi$ photons cm^{-2} s^{-1} sr^{-1} or 2.41×10^{-7} ergs cm^{-2} s^{-1} sr^{-1} at Hα.

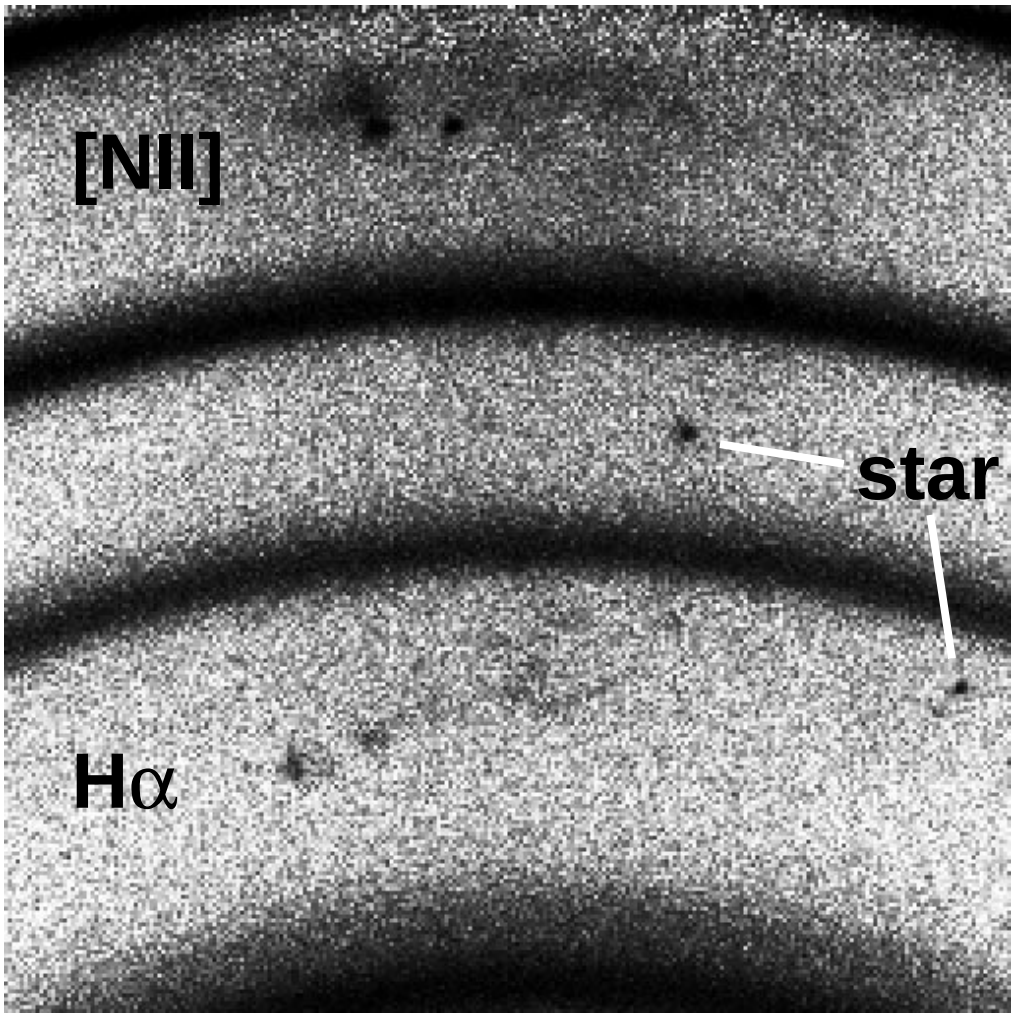

FIG. 3.—Magnified image of part of the SW3 field in Figs. 1 and 2. The field of view is rotated so that the vertical axis lies parallel to the galaxy major axis. Clumpy [N II] and Hα emission is clearly visible. What is not easily rendered is the diffuse emission between and at large off-axis angles to the major axis. Notice the extremely faint galaxy continuum ($B \sim 25$ mag arcsec^{-2}) over much of the field. The bright arcs are atmospheric OH lines.

flaring resulting from the declining stellar surface density (Olling 1995), which tends to reduce the projected emission measure. To minimize the velocity spread, we rotate the instrument so that the incomplete ring pattern is convex in the same sense as the projected velocity field and is centered on the kinematic major axis (see Figs. 1 and 2).

4. REDUCTION AND ANALYSIS

A detailed discussion of the many subtleties of data analysis is to be presented elsewhere; a brief overview is given here. An important step is establishing the optical axis of the incomplete calibration rings to better than 0.1 pixel. This was achieved with orthogonal distance regression (e.g., Boggs, Byrd, & Schnabel 1987). Next, we azimuthally bin the calibration rings for all nights to ensure that (*a*) there were no optomechanical shifts, (*b*) the instrumental response was constant, and (*c*) the etalon-gap zero point was constant from night to night. With respect to point *b*, the etalon was found to behave reliably, except that there was a slow drift in the optical gap during the first night.

Some calibration spectra showed baseline variations after binning over different parts of the field. This arises from illumination (vignette) effects, stray light, chip structure, and CCD fringing, which can be divided out reliably with flat fields. The spectral bandpass seen by individual pixels is roughly 1 Å where the bandpass centroid declines by 40 Å from the optical axis to the field edge. Twilight flats were found to be the most reliable, although the Fraunhofer spectrum leaves its imprint on the data. We divide out the solar spectrum from the flat field by establishing the mean spectrum and then generating a polar image with this spectrum. Occasionally, the flat fields leave residual fringe structure in the data. It is possible to remove this with azimuthal smoothing, but potentially informative intensity variations in the data would be washed out. CCD fringing constitutes the main systematic error in diffuse detection and provides a major challenge to achieving deeper detection limits than that quoted by BTVS. The response of the blocking filter is removed in the twilight division.

To obtain discrete spectra from the summed CCD images, the data were divided into annular rings that were two pixels wide. Within each annulus, we can calculate the mean, median, or mode of the histogram. Cosmic-ray events appear as outliers and are therefore easily removed. We tried more sophisticated methods (e.g., the biweight statistic), but the improvement was found to be marginal. The weak underlying galaxy continuum observed in NGC 253 had only a negligible effect on the final spectra. This was

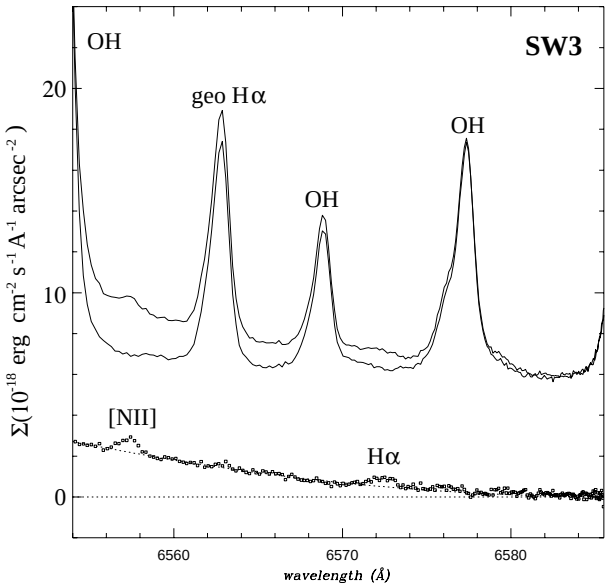

FIG. 4.—Emission-line spectrum at the H I edge (field SW3 in Figs. 1 and 2) compared with the off-field spectrum. The difference of these spectra is shown below. Remarkably, the [N II] λ6548 line has a surface brightness comparable to the Hα surface brightness, as compared to solar-abundance H II regions, where the ratio is an order of magnitude smaller. This result holds after removing the dense knots in Fig. 3. The azimuthally averaged galaxy continuum underlies the spectrum and corresponds to roughly $\mu_B = 23$ mag arcsec^{-2} below [N II], falling to 25 mag arcsec^{-2} below Hα. The equivalent widths of the lines are 0.60 and 1.8 Å, respectively.

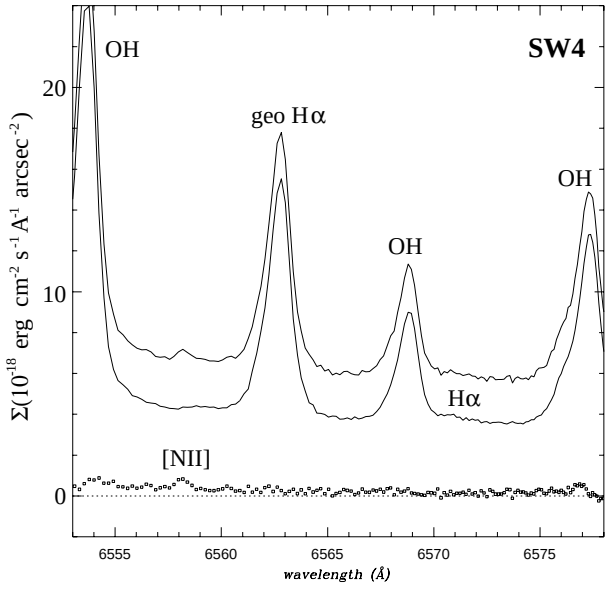

FIG. 5.—Emission-line spectrum for the field beyond the H I edge (field SW4 in Figs. 1 and 2). As we did not get a matching sky exposure, the spectra are shown from binning over two different opening angles. The top spectrum results from binning over 25° about the major axis from the optical axis; the lower spectrum arises from binning over the entire field. The difference of these spectra is shown below. The [N II] emission is clearly seen in the top spectrum and, indeed, in a high-contrast image. This line is completely washed out in the lower spectrum. The Hα emission is just visible in the high-contrast image and does not begin to appear until we sum over the entire field. The difference has been taken after weighting the top spectrum for its lower signal-to-noise ratio. Again, we see a very faint galaxy continuum spectrum that is roughly $\mu_B = 26$ mag arcsec^{-2} after azimuthal binning below the [N II] line, dropping to $\mu_B = 27$ mag arcsec^{-2} below the Hα line. The equivalent widths of the lines are 7.8 and 9.9 Å, respectively.

examined by subtracting a matching *R*-band exposure, modulated by the polar response of the blocking filter. This same image was used to identify unresolved sources within the field.

Sky subtraction is particularly hazardous, since atmospheric humidity produces variable water vapor features. If the object fills the field of view, as does NGC 253, it is necessary to obtain off-field exposures at the same air mass and at comparable humidity. The OH lines are time variable, but, most importantly, they vary with the zenith angle of the observation (Kondratyev 1969). This is quite distinct from the geocoronal lines, which reach a minimum at local midnight, rising sharply toward dawn. The night-sky lines allow for wavelength calibration to better than 0.04 Å (Osterbrock & Martel 1992), as shown by the difference in wavelength produced by a discharge lamp and solar Lyβ resonance excitation of the exosphere (Yelle & Roesler 1985). The velocity centroid of the Galactic [N II] emission ("Reynolds layer"), using new wavelengths from Spyromilio (1995), provides an independent measurement of the Earth-Sun motion with respect to the local standard of rest. For all four nights, the conditions were consistently photometric, as judged by the Reynolds-layer emission. The photometric calibration was achieved using both line and continuum flux standards (Table 1).

5. RESULTS

The four TAURUS-2 field positions are shown in Figures 1 and 2, overlaid on a *B* image of NGC 253 and its deepest H I image to date. A magnified section of one interferogram is shown in Figure 3, and summed spectra are shown for the two outermost fields in Figures 4 and 5. The staring method allows for an extremely deep spectroscopic detection over pixels that fall within the projected arc defined by a discrete frequency. There are two frequencies of interest, so kinematic measurements are possible at two positions within each field. The etalon was tuned to two different spacings for the innermost field, so that we have kinematic measurements at no more than 10 independent positions along the major axis. These data are presented in Figures 6 and 7.

Optical line emission is detected in all field positions. In fields SW1 and SW2, bright H II regions were clearly seen in both Hα and [N II] λ6548. These short exposures were taken in order to establish the systemic velocity of the gas independently. The kinematic measurements are seen in Figure 6*c* at $r < 7'$. The large systematic errors in both axes are caused by averaging azimuthally over a large spread in velocities and radial distances within the projected plane at small galactic radii.

Field SW3 is the imf defined by the criterion in equation (7). Weak stellar continuum emission is seen over the central third of the field, extending from roughly $\mu_B = 23$ mag arcsec^{-2} (northeast) to 25 mag arcsec^{-2} (southwest). The [N II] and Hα line emission comprise clumpy structure superimposed on a faint, diffuse component. Only two of the sources are unresolved: these show up on our matched *BVR* images and are labeled in Figure 3. The two bright knots at the position of the [N II] line are probably faint H II regions.

The summed spectrum for field SW3 is shown Figure 4. The difference of the on-object and off-object spectra clearly shows the declining stellar disk along the major axis, in addition to the [N II] and Hα lines at 6557.7 and 6572.8 Å.

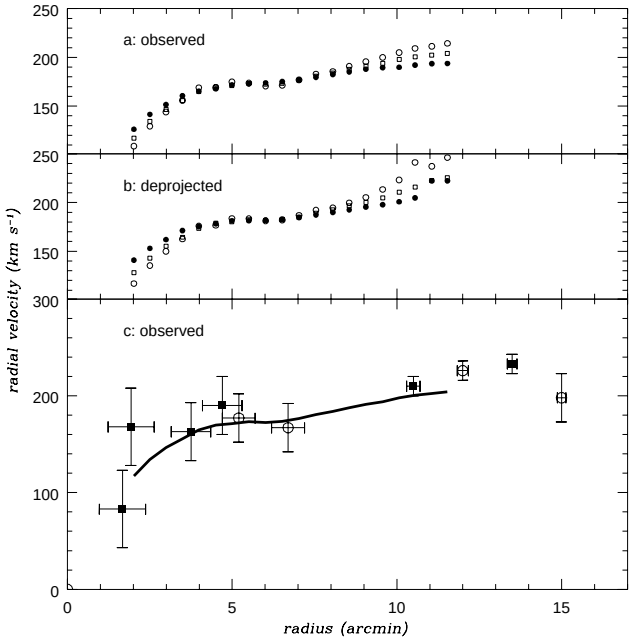

FIG. 6.—Kinematic measurements along the major axis of NGC 253, deduced from VLA H I, TAURUS-2 Hα, and [N II] lines. (*a*) Original rotation curve of PCvG has been projected onto the sky with their inferred orbit inclination at each radius. Three sets of measurements are shown: these represent the approaching side (*open circles*), receding side (*squares*), and fit to the full velocity field (*filled circles*). (*b*) PCvG's original curves, where the data have been deprojected with the measured inclination at each radius. (*c*) Solid line is the same curve as the squares in (*a*). The filled squares are the TAURUS-2 [N II] measurements; the circles are the Hα measurements.

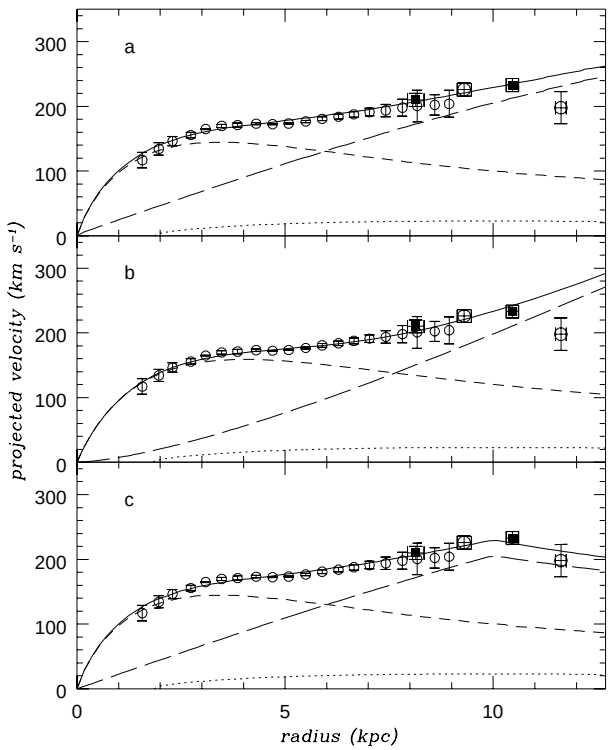

FIG. 7.—Representative fits to the PCvG and TAURUS-2 data using a three-component mass model (disk, halo, and gas). The contribution from the H I surface density (*dotted line*) is the same in all models. (*a*) We adopt an exponential disk (*short-dashed line*) and an isothermal sphere for the spherical halo (*long-dashed line*), using the numerical approach developed by Carignan (1985). (*b*) We have used the disk-halo models of Dehnen & Binney (1997): the least-squares fit was carried out by W. Dehnen. (*c*) We have truncated the halo at a radius of 10 kpc in order to demonstrate a possible explanation for the last measured point.

While these lines fall at different spatial locations within the galaxy, the strength of the blue [N II] line with respect to Hα is striking, a result that holds after removing the bright knots. The weakness of the galaxy continuum rules out a significant correction to the Hα line flux resulting from stellar absorption (Bica & Alloin 1987). We achieved the same basic result in the 1995 September 27 observations, although the signal-to-noise ratio was roughly half that of the earlier observations. Both sets of observations show that the diffuse emission peaks toward the major axis.

The summed spectrum for field SW4 is presented in Figure 5. This field lies beyond the H I edge of NGC 253. Unfortunately, we did not manage to obtain a matching sky observation. The data clearly show weak [N II] emission and possibly broad diffuse Hα emission. We have attempted to subtract something approximating a background spectrum by dividing up the field into three vertical panels that have equal area when the outer panels are taken together. The central section constitutes our on-object spectrum, the outer quarter panels our off-object spectrum. The weak outer envelope of the galaxy is seen in the difference spectrum. The [N II] emission peaks toward the major axis and is not detected in the outermost panels. Broad diffuse Hα emission is seen in both regions at comparable intensity and therefore subtracts cleanly in the residual spectrum. That this feature is real can be seen by comparing the lower spectrum in Figure 5 with the off-object spectrum in Figure 4, where such a feature is not seen.

The radial velocities for the emission lines in Figures 4 and 5 were corrected for Earth's motion before subtracting the systemic velocity of NGC 253. These measurements are presented in Figures 6 and 7. The innermost TAURUS-2 measurements were used to establish the systemic velocity of the ionized gas. Schommer et al. (1993) show the systematic uncertainties that can arise between H I and ionized gas kinematics. Our optical determination (243 ± 9 km s^{-1}) is consistent with the weighted-average H I measurements (249 ± 8 km s^{-1}) from the NASA/IPAC Extragalactic Database. We adopt the H I value 245 ± 5 km s^{-1} (Puche, Carignan, & van Gorkom 1991, hereafter PCvG), as we wish to relate the optical data to their data. For the measurements between $r = 10'$ and $r = 14'$, the kinematic error is dominated by the uncertainty in systemic velocity. The smaller error bars compared to the inner TAURUS-2 measurements reflect the smaller intrinsic radial and kinematic dispersion. The fact that the optical values appear to be systematically high by 10 km s^{-1} is discussed in the next section. For the outermost point, the diffuse broad feature has a large kinematic measurement uncertainty. Unlike the other lines, this feature has fairly uniform intensity over the full field. Its lack of continuity with the other measurements calls into question its association with the galaxy.

6. DISCUSSION

6.1. *Dynamical Interpretation*

The major-axis measurements in NGC 253 pose an interesting problem. In Figure 6 the "rotation curve" appears to flatten off before rising at a radius $r = 7'$. This effect is seen for both the approaching and receding sides of the disk, with (Fig. 6*b*) or without (Fig. 6*a*) the correction for orbit

inclination. In Figure 6*c*, the TAURUS-2 measurements confirm and extend this trend out to $r = 13.'5$. The outer TAURUS-2 values are somewhat higher than the azimuthally averaged H I rotation curve, but this is a distinctive feature of the approaching side of the disk (Fig. 6*a*) in that the outer H I measurements here are higher than average.

If we assume that the distribution of mass has spherical symmetry, then from Poisson's equation,

$$\frac{d}{dr}(rv_c^2) = 4\pi G r^2 \rho(r) , \tag{8}$$

where ρ and v_c are the local mass density and the circular velocity. For the flat region of v_c, ρ declines as r^{-2}; the sudden rise requires the density profile to become much flatter or even constant with increasing radius. A slightly flattened potential gives the same result, although the inferred total mass will be overestimated in this case.

The inflection in the rotation curve can be understood naturally as arising from the potential of an exponential stellar disk with a much larger dark halo (e.g., Carignan & Freeman 1985). To illustrate this, we show a variety of possible three-component fits to the data.

In the first model (Fig. 7*a*), the H I and stellar disks have the same form. The dark halo is represented by an isothermal sphere, which is fully specified by any two of the halo central density ρ_h, the central velocity dispersion σ_h, or the core radius r_h. The stellar disk is specified by a central surface density μ_e and a scale length r_e. The H I surface density profile is given in PCvG (Fig. 5); the central hole within $r = 1.'9$ causes the gravitational force resulting from the gas to be directed outward (e.g., Staveley-Smith et al. 1990). We have taken $\sigma_h = 253$ km s^{-1}, $r_h = 18$ kpc, $\mu_e = 1.35 \times 10^9\ M_\odot$ kpc^{-2}, and $r_e = 1.6$ kpc. These values compare well with those of PCvG, except that the disk and halo scale lengths are 30% smaller than their values. In order to match the observed data, the model rotation curves have been projected to a plane inclined at 72°. We note that such a large core radius is normal for the dark halo of large disk galaxies (e.g., Freeman 1993).

In the second model (Fig. 7*b*), the radial forms of the disk and halo are given by Dehnen & Binney (1997). For the halo, we adopt

$$\rho_h(R, z) = \rho_0 \left(\frac{m}{r_0}\right)^{-g} \left(1 + \frac{m}{r_0}\right)^{g-b} \exp\left(\frac{-m^2}{r_t^2}\right), \tag{9}$$

with

$$m^2 = R^2 + (z/q)^2 . \tag{10}$$

The halo parameters are the halo density normalization, ρ_0, the halo scale radius, r_0, the outer cutoff radius, r_t, and the inner and outer power slopes, g and b. Apart from the halo axis ratio ($q = 0.8$), all of these parameters were obtained from a fit to the rotation curve. Both the stellar and gaseous disks are assumed to be exponential in form, i.e.,

$$\rho_d(R, z) = \frac{\mu_d}{2z_d} \exp\left(-\frac{R_m}{R} - \frac{R}{R_d} - \frac{|z|}{z_d}\right). \tag{11}$$

For each of the disks, the adopted parameters are the surface density normalization, μ_d, the disk scale height, z_d, and the disk scale radius and inner cut-off radius, R_d and R_m. For the H I disk, these were fixed at $\mu_d = 1.94 \times 10^7\ M_\odot$ kpc^{-2}, $R_d = 3.92$ kpc, $z_d = 0.04$ kpc, and $R_m = 1.22$ kpc. For the stellar disk, $R_d = 1.80$ kpc, $z_d = 0.15$ kpc, and $R_m = 0$ kpc, as suggested by the photometry. The surface-density normalization for the stellar disk was obtained from the least-squares fit.

The fit, kindly undertaken by W. Dehnen, ignored the last TAURUS-2 measurement to yield the following results: $\mu_d = 1.56 \times 10^9\ M_\odot$ kpc^{-2}, $\rho_0 = 1.98 \times 10^8\ M_\odot$ kpc^{-3}, $g = -1.058$, $b = 1$, $r_0 = 34.2$ kpc, and $r_t = 164.0$ kpc. Of these, b was constrained to be greater than or equal to unity. Figure 7*b* shows that the rising halo contribution to the rotation curve gives a better fit to the data overall. But there are strong correlations between the various parameters, and the fitted results depend critically on which of the TAURUS-2 points are included.

The outermost TAURUS-2 Hα measurement in Figures 6*c* and 7 suggests that the rotation curve may be falling beyond a radius of about 10 kpc, but there are certainly other possible explanations for its low observed velocity. For example, (i) it may result from tidal distortion of the outermost regions of NGC 253, or (ii) it may result from accretion of a faint gas-rich object at large radius. In support of the accretion idea, a stacked photographic image by D. Malin shows extended stellar light at faint levels ($\sim$26 mag arcsec^{-2}) to the southwest of the disk; similar emission is not seen to the northeast. (iii) While the emission may arise from an outer ionized envelope, it is conceivable that this emission is associated with the group itself. An extragalactic H^+ cloud has recently been discovered in the Fornax cluster (Bland-Hawthorn et al. 1995). Mathewson, Cleary, & Murray (1975) and Arp (1985) found tentative evidence for H I clouds within the Sculptor group (cf. Haynes & Roberts 1979). It is difficult, however, to reconcile the Hα radial velocity ($\approx$440 km s^{-1}) with the Magellanic Stream, which passes in front of the Sculptor group (Mathewson & Ford 1984).

Finally, we consider the possibility that the rotation curve of NGC 253 is indeed falling beyond 10 kpc. Such a rapid decrease suggests that the dark halo may be truncated. We can illustrate the effect of such truncation with a simple model. We take the halo density distribution to be

$$\rho_h = \rho_0 (1 + r^2/r_a^2)^{-1} , \tag{12}$$

with the rotation curve $V(r)$ given by

$$V^2 = V_\infty^2 \left[1 - \left(\frac{r_a}{r}\right) \tan^{-1}\left(\frac{r}{r_a}\right)\right]. \tag{13}$$

For $V_\infty = 733$ km s^{-1} and core radius $r_a = 18$ kpc, the rotation curve for this model is very similar to that of the isothermal halo in Figure 7*a*: the optical galaxy lies well within the core radius of the halo, and the halo rotation curve is close to solid body. We now truncate the halo at $r = 10$ kpc; its rotation curve is then Keplerian for $r > 10$ kpc. Figure 7*c* shows how the resulting total rotation curve now provides an acceptable fit to all of the H I and TAURUS-2 data. The model is artificial (the halo is sharply truncated, and we did not truncate the stellar and H I disks), but the point is obvious enough: truncation of the dark halo near the observed outer edge of the H I disk can produce the apparent falling rotation curve.

If this is all correct so far, there are some interesting consequences. The properties of dark halos are best studied in disk galaxies for which the H I distribution extends well beyond the optical distribution. In the outer regions of these galaxies, the ratio of dark matter surface density to H I

surface density is roughly constant (e.g., Bosma 1978; Carignan 1991). NGC 253 is not such a galaxy. Its H I extent is similar to its optical extent (e.g., PCvG). Our data provide the first hint that in galaxies like NGC 253, where the H I and the light are coextensive, the dark matter may also not extend much beyond the optical distribution. It is tentative evidence of the apparent link between the dark matter and the H I. We emphasize that the dark matter is still essential for generating the observed rotation curve for NGC 253: the inferred mass ratio of dark matter to luminous matter is about 5. Our point is simply that the dark matter distribution in NGC 253 may be truncated at a radius of only 10 kpc, compared to the much larger dark halo distributions observed in our Galaxy (e.g., Freeman 1996) and other large spirals (e.g., Zaritsky et al. 1997).

The reduced χ^2 values for the models presented in Figures 7*a* and 7*b* are 5.2 and 2.9, respectively. The latter model has the highest statistical significance of all models, but the basic assumptions are unlikely to be physical. A flat rotation curve given by equation (13) does not fit the measurements adequately. The reduced $\chi^2 = 6.3$, and, more significantly, 10 of 12 points outside of $r = 7'$ miss the curve by more than 2 σ. But the inclusion of a truncation radius lowers the reduced χ^2 to 3.9, and the curve now passes through all the outer points (Fig. 7*c*).

6.2. *Ionization and Heating of the Diffuse Gas*

The most striking feature of the spectra presented in Figures 4 and 5 is the inferred high [N II] λ6548/Hα ratios. To ensure that the white-light calibration adequately removed the filter response over the field (§ 4), we examined the line ratios in H II regions over the inner disk. Where we have two interference rings that fall close together on the sky—one from Hα, the other from [N II]—the H II regions appear weak in [N II], compared to Hα, which is indicative of the order-of-magnitude difference expected for inner-disk H II regions. If the outer H I gas has subsolar abundances (Pagel 1989; Diaz 1989), the enhanced line ratio must arise from one or more excitation processes. To date, however, numerical models involving a single ionizing source have not managed to produce such an enhancement (e.g., Sokolowski 1994). Thus, we separate our discussion of ionization and excitation where possible. Almost certainly, the anomalous ratio is indicative of a higher local electron temperature, for which there are various mechanisms. In solar-abundance H II regions, this ratio rarely exceeds 0.15 (Evans & Dopita 1985): increasing this ratio substantially requires that we selectively heat the electrons without producing N^{++}.

The required ionizing flux.—The emission measure $\mathscr{E}_m$ from the surface of a cloud embedded in a bath of ionizing radiation gives a direct gauge, independent of distance, of the intensity of the ambient radiation field beyond the Lyman continuum (Lyc) edge (e.g., Hogan & Weymann 1987). This assumes that the covering fraction *seen by the ionizing photons* is known and that there are sufficient gas atoms for soaking up the incident ionizing photons. At electron temperatures of 10^4 K, collisional ionization processes are negligible. Perpendicular to the surface, from equation (1), the column recombination rate in equilibrium must equal the incident ionizing photon flux, $\alpha_B n_e N_p = \varphi_i$, where φ_i is the rate at which Lyman continuum photons arrive at a planar cloud surface (photons cm^{-2} s^{-1}), and N_p is the column density of ionized hydrogen. The emission measure produced by this ionizing flux is

$$\mathscr{E}_m \approx 4.5\varphi_4 \text{ mR} , \quad (14)$$

where $\varphi_i = 10^4\varphi_4$ (Bland-Hawthorn & Maloney 1997, hereafter BM). For an optically thin cloud in an isotropic radiation field, the solid angle from which radiation is received is $\Omega = 4\pi$, while for one-sided illumination, $\Omega = 2\pi$. However, φ_i can be anisotropic, and Ω can be considerably less than 2π.

Metagalactic ionizing background.—The measured surface brightness values for the emission lines in Figures 4 and 5 are as follows: for the [N II] λ6548 line, 90 ± 5 mR ($r = 10'.5$), 46 ± 5 mR ($r = 12'.0$); for the Hα line, 81 ± 6 mR ($r = 13'.5$), 41 ± 8 mR ($r = 15'.0$). If the underlying H I is optically thick to the Lyman continuum, the Hα lines require an ionizing flux of 2×10^5 and 9×10^4 photons cm^{-2} s^{-1}. The present upper limit on the metagalactic ionizing flux (§ 3.1) is $J^0_{-21} < 0.08$ ergs cm^{-2} s^{-1} Hz^{-1} sr^{-1} (2 σ), which sets an upper limit on the one-sided ionizing flux, at the surface of an optically thick H I sheet, of 2×10^4 photons cm^{-2} s^{-1}, thereby ruling out the metagalactic background as the dominant ionizing source. The combined ionizing radiation from hot gas and galaxies within the Sculptor group is also much too weak. Sciama (1995) predicts an ionizing flux that is an order of magnitude higher from decaying neutrinos, which could conceivably account for much of the Hα flux. However, the narrow energy bandpass of decaying neutrinos (Sciama 1996) at the Lyman limit cannot produce N^+ and therefore requires an additional source of ionization.

Compact halo sources.—The most recent summary of the MACHO project indicates that as much as half of the dark matter in the Galaxy out to the LMC is made up of solar-mass objects. There is wide disagreement on whether the missing mass could comprise a halo population of white dwarfs (Adams & Laughlin 1996; Kawaler 1996; Chabrier, Segretain, & Méra 1996). But most plausible models invoke a population that produces essentially no UV flux. This is supported by high-redshift observations of the precursor halo population (Charlot & Silk 1995).

Compact disk sources.—Unlike ellipticals, spiral galaxy disks tend not to "grow" when photographic plates are stacked or amplified to reveal light at very faint levels (Malin 1983). But a photographically amplified plate of NGC 253 (Malin 1981) reveals a faint blue disk extending to the limits of our outermost detection ($r = 15'$). Following a suggestion from G. B. Field, we now consider whether these could comprise an extended white dwarf population (including the precursor population of central stars in planetary nebulae) young enough to produce a significant UV disk flux. Such a population was originally considered by Lyon (1975) and Bania & Lyon (1980). In Figure 8, we consider whether white dwarfs could account for the diffuse line emission in concert with the faint stellar continuum at the H I edge in NGC 253 (*barred arrow*). We present the expected Hα emission measure $\mathscr{E}_m$ versus B surface brightness for an isothermal population of white dwarfs as a function of the disk surface density. The contribution to both of these quantities from white dwarfs in the solar neighborhood is also shown (*filled symbols*). The luminosity function is taken from Liebert, Dahn, & Monet (1988) and the luminosity-temperature conversion from Wood (1990).

There are two basic problems in using white dwarfs to explain the disk ionization. In the solar neighborhood, the

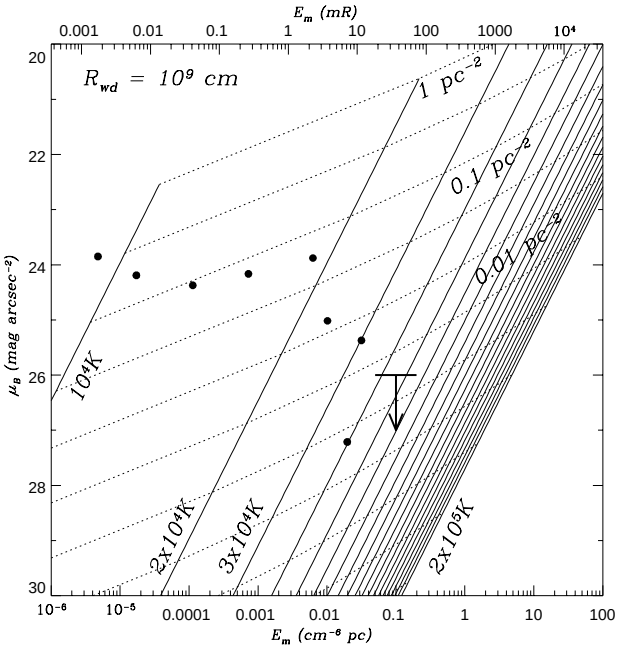

FIG. 8.—Predicted Hα emission measure $\mathscr{E}_m$ vs. B surface brightness for an isothermal population of white dwarfs as a function of surface density. The solid lines are isotherms for white dwarf temperatures in the range 10^4–2×10^5 K. The dashed lines are isochoric lines indicating variations in white dwarf surface density in steps of 0.5, in dex, starting at 1 pc^{-2} at the top. The arrow indicates the average emission measure and disk–surface brightness upper limit at the edge of the H I disk. The filled circles are the expected contribution to the B-band flux and Hα emission measure for the white dwarf population in the solar neighborhood (assuming that all photons are absorbed). The Galactic disk is assumed to be 600 pc thick, and the white dwarf radius is assumed to be 0.14 $R_\odot$.

combined effect of all white dwarfs could produce $\mathscr{E}_m = 0.1$ cm^{-6} pc, which fails to explain the Reynolds-layer emission by an order of magnitude or more, in agreement with Nordgren, Cordes, & Terzian (1992). If we assume a comparable star formation history in the outer reaches of NGC 253, this model could conceivably be used to explain the measured Hα emission. This is particularly attractive in that the high temperatures of the white dwarf population produce elevated [N II]/Hα ratios (Sokolowski & Bland-Hawthorn 1991). However, if the luminosity function resembles the solar neighborhood, the combined disk surface brightness at B from the cooler white dwarfs is very much brighter than what is observed, particularly when one includes the contribution of early main-sequence stars. Alternatively, attempting to explain the low Hα emission measure in terms of 2000 white dwarfs kpc^{-2} at 45,000 K leads to a timing problem. We have measured an age-temperature relation from Wood (1990) for which

$$\log\left(\frac{t}{\mathrm{yr}}\right) = 3.6 \log T_{\mathrm{wd}} - 9.7 \,. \qquad (15)$$

Stars hotter than 40,000 K have left the asymptotic giant branch less than 10^7 yr ago, which would require a highly contrived star formation history throughout the disk.

S. G. Ryan has suggested the possibility of hot, horizontal-branch stars, in particular, an isothermal population with temperatures around 15,000 K (Lee 1993). If we assume comparable line blanketing with white dwarfs, Figure 8 illustrates that such a population will always produce too much blue light for the required ionizing flux, irrespective of the uncertain sizes and surface densities of both objects. The characteristic "temperature" of the ionizing source needs to be sufficiently high to fall within the strict B-band limit. Interestingly, this is just what is needed to enhance the [N II]/Hα ratio significantly, as photons with higher mean energies produce higher electron temperatures.

Ram pressure heating.—Mathis (1986) has stressed the problems associated with shocks as a source of ionization and heating for the Reynolds layer, particularly that of the near-uniformity of the emission. An interesting possibility is ram-pressure heating, as NGC 253 moves through an external medium in which the disk is inclined at some angle to its direction of motion. The wake of NGC 7421 (Ryder et al. 1996) suggests that such a process can take place. To ionize a column of 10^{19} atoms cm^{-2} requires shock speeds of close to 130 km s^{-1} (Dopita & Sutherland 1996). A medium with preshock density $\sim 10^{-2}$ cm^{-3}, moving through an ambient medium with the relatively high density $\sim 10^{-3}$ cm^{-3} at 400 km s^{-1}, could produce the necessary ram pressure. The postshock temperature at a shock velocity of 130 km s^{-1} is 2.4×10^5 K, which is a factor of 10 higher than the upper limit from the Doppler parameter (22 km s^{-1}) of the observed line profiles. For N^+ and H^+ to have been collisionally ionized, the gas must have had time to cool. But groups with low velocity dispersions, like the Sculptor group, tend to have very little intracluster medium (Fadda et al. 1996). Therefore, the galaxy would need to be running into a large, external gas cloud for the shock model to remain plausible.

Exotic heat sources.—There exists a wide range of exotic models for heating the electron population preferentially, including turbulence-driven MHD wave heating (Raymond 1990) and mixing layers driven by bulk flows (Slavin, Shull, & Begelman 1993). Bulk flows and turbulence in the disk are thought to be maintained primarily by energy injection from star formation. The star formation rates at the H I edge are likely to be very small. An alternative possibility is that the outer disk is being rained on by galactic fountain material driven by the inner starburst (e.g., Benjamin & Shapiro 1993). It is unclear at present whether fountain models can generate the necessary heating through shocks. Ferland & Mushotzky (1984) have shown that under rather special conditions, low-energy cosmic-ray electrons can selectively heat ions and electrons through Coulomb repulsion. However, Sciama (1996) emphasizes the difficulties involved in the penetration of gas clouds by cosmic rays, and these do not appear to be an important agent.

Young stellar disk.—The inner disk of NGC 253 hosts a young stellar population producing copious amounts of ionizing photons. It is plausible that the outer disk sees this radiation either through dust scattering or through warps in the outer parts. For Rayleigh scattering, we have repeated the calculations of Jura (1980) using up-to-date dielectric phase functions (Martin & Rouleau 1990; Draine & Lee 1984) and assuming a standard grain mixture and distribution (Mathis, Rumpl, & Nordsieck 1977). We adopt the Henyey-Greenstein (1941) phase function, which relates the asymmetry parameter g to photon energy. The expected ionizing flux at the H I edge is much less than 10^5 photons cm^{-2} s^{-1}, primarily because of the highly forward-scattering behavior ($g > 0.9$) of the grains at increasing energy, toward the Lyman limit.

While there is some uncertainty as to the fraction of ionizing photons that escape a normal spiral galaxy, two independent lines of argument suggest that roughly 5% of

ionizing photons escape the Galaxy (Domgörgen & Mathis 1994; BM). The absolute B magnitude of NGC 253 is comparable to that inferred for the Galaxy, and thus, if the disk opacity is comparable in both cases, the models in BM apply here as well. G. D. Bothun (1997, private communication) suspects that the disk of NGC 253 may be more opaque than the Milky Way, in which case our predicted fluxes should be considered as upper limits. To explain the Hα flux at both outer positions (9 and 12 kpc) requires an integral sign warp originating at 7 kpc and reaching 20° at 10 kpc. It is difficult to rule this out on the basis of the H I data. At face value, Figure 8 of PCvG indicates that such a warp starts at 7 kpc, reaching $\approx 10°$ at 9 kpc. In the next section, we explore this model in more detail.

Dilute photoionization.—After Sokolowski (1994), we attempt to simulate conditions at the H I edges of spiral galaxies ionized by the stellar radiation field from the central disk. This requires that the outer southwestern edge of NGC 253 be warped ($\sim 25°$) or flare up and therefore see the central regions. We use the CLOUDY code (Ferland 1991) to ionize plane-parallel slabs with cosmic abundances (Grevesse & Anders 1989). The physical state and emission spectrum of a low-density photoionized gas with a given composition are fixed by two parameters: the shape of the ionizing continuum and the ionization parameter (Tarter, Tucker, & Salpeter 1969). For the ionization parameter U (the ratio of ionizing photons to nucleons), we adopt

$$U = \frac{\varphi}{cn_{\rm H}}, \tag{16}$$

where c is the speed of light. In Figure 10, the results for a range of emission-line diagnostics are presented as a function of U. The radiation-bounded models are truncated

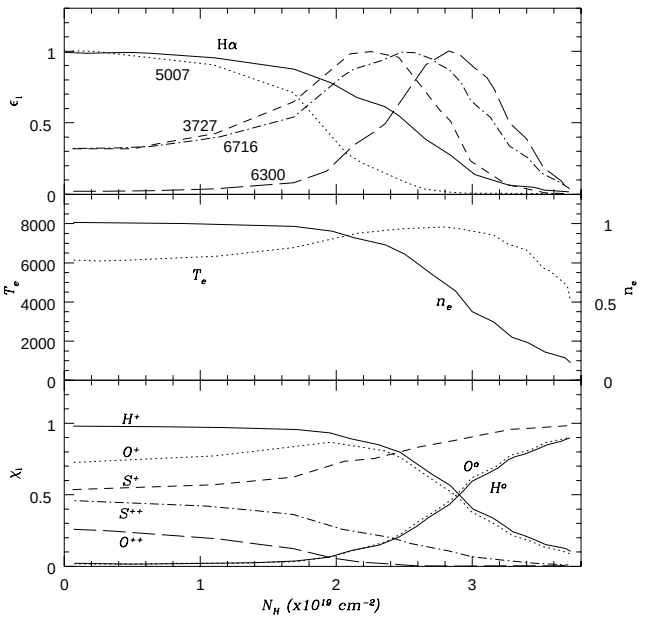

FIG. 9.—Lower panel shows the relative ionization fraction of important neutrals and ions, where the front of the gas slab ($N_{\rm H} = 0$) is ionized by a dilute radiation field ($U \sim 10^{-4}$). The middle panel shows the temperature and mean electron density structure within the slab. The top panel shows the normalized line emissivities and illustrates the relative dependence on electron temperature, electron density, and ionization fraction.

when the electron temperature T_e falls below 4000 K; all models assume $n_{\rm H} = 1\ {\rm cm}^{-3}$.

The unabsorbed radiation field is a composite, taking the form $\psi_c \xi(M_*) t(M_*)$, where ψ_c is the current star formation rate, ξ is the initial mass function, and t is the main-sequence lifetime. The ionizing field is dominated by stars with $M_* \geq 40$; we specify the upper mass cutoff to be $M_* = 120\ M_\odot$. The stellar atmospheres are from Mihalas (1972) and Kurucz (1979); the solar-metallicity evolutionary tracks are from Maeder (1990). For the massive star initial mass function, we adopt $\xi(M_*) \propto M_*^{-2.7}$, which falls between the Salpeter (1955) and the Miller-Scalo (1979) models.

Irrespective of the *shape* of the ionizing continuum, a dilute radiation field leads to enhanced emission from low-ionization emission lines (Ferland & Netzer 1983; Halpern & Steiner 1983). But a general hardening of the ionizing field also produces the same trend (e.g., Sokolowski & Bland-Hawthorn 1991). Indeed, if the edges of spirals are ionized by the central stellar disk, the ionizing field is expected to be both dilute and hardened.

There are at least two phenomena that serve to harden the local ionizing radiation field: interstellar opacity and metal depletion (i.e., refractory elements) onto grains. We assume that the ionizing photons have leaked from the young inner disk and that the ionizing spectrum has been hardened by intervening absorption ($\tau_{\rm LL} \sim 3$ perpendicular to the disk). We adopt the atomic photoionization cross section for which the average interstellar opacity varies as $E^{-2.43}$ above 13.6 eV (Cruddace et al. 1974). In quiescent galaxies, the outer H I disk is expected to have subsolar metallicities (e.g., Molla, Ferrini, & Diaz 1996). But the ongoing nuclear starburst in NGC 253 (Beck & Beckwith 1984; Antonucci & Ulvestad 1988) could conceivably enrich the outer disk through long-range galactic fountains (Corbelli & Salpeter 1988). On balance, we adopt solar abundances (Grevesse & Anders 1989) modified by the known depletion rates for cold gas (Cowie & Songaila 1986; Jenkins 1987; Savage & Massa 1987).

Gas-phase depletion.—The formation of grains primarily depletes Ca, Fe, and Si, which in turn suppresses the dominant coolants from the singly ionized stages of these atoms (Ferland 1992). For example, at $U = 10^{-4}$, [C II] 158 μm and [Si II] 35 μm account for one-quarter of the total nebular cooling. While C, N, and O are not strongly depleted, the forbidden line emission from N^+, O^0, O^+, and O^{++} is greatly enhanced by the increased temperature. In particular, Mathis (1986) finds that the [N II]/Hα ratio increases as $T_e^{3.6}$. Therefore, a 20% increase in the local electron temperature can effectively double this line ratio. We neglect grain heating and cooling processes (Reynolds & Cox 1992), as these are only important in the high-U limit (Baldwin et al. 1991; Ferland 1992). Complete removal of the grain population from the depleted gas causes line strengths to change by no more than 5% (Shields 1992).

Photoionization models.—In Figure 9, we show the detailed ionization and thermal structure within the gaseous slab. N^0, O^0, and H^0 are closely coupled with slight differences caused by charge-exchange reactions. N^+, O^+, and H^+ are therefore also closely linked, but divergence can occur at the front of the slab if the radiation field is sufficiently strong to produce a higher state of ionization in N or O. The soft photons are soaked up and fully ionize the front of the slab; the harder photons propagate further into the

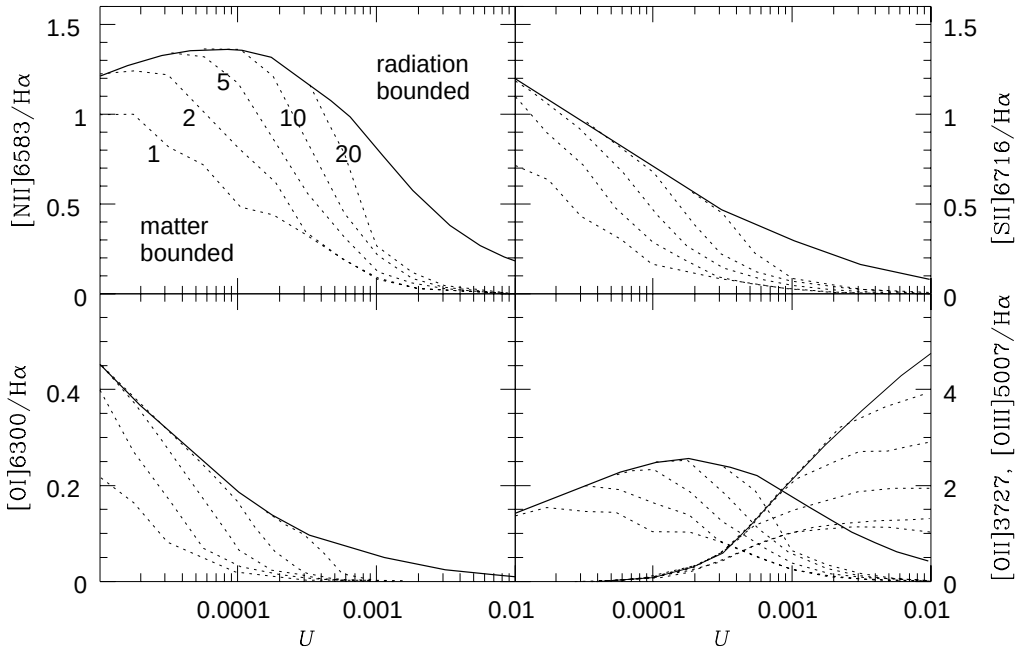

FIG. 10.—Dependence of five important line diagnostics on the strength of the radiation field and hydrogen column density. The solid lines are radiation-bounded models, where all ionizing photons are soaked up by the gas. Also shown are matter-bounded models, where the slab has been truncated at 1, 2, 5, 10, and 20 $\times$ 10^{18} cm^{-2}. The observed line ratio [N II] λ6548/Hα is a factor of 2.98 smaller than [N II] λ6583/Hα (Veilleux 1988). Fig. 9 gives some appreciation for the distinct trends shown by different lines (e.g., [O II] vs. [O III]).

gas and set up a partially ionized zone. Here the electron temperature increases by 25%, which boosts the emissivities of the [O I], [O II], [N II], and [S II] lines. The high-energy photons are essential: cutting off the continuum just below the ionization potential of N II (29.6 eV) produces [N II] λ6548/Hα line ratios that are no higher than 0.25.

Figure 10 shows the dependence of five important line diagnostics on both ionization parameter and the gas column density. The range of column densities shown are relevant to spiral edges. The line ratio [N II] λ6583/Hα peaks at $U = 10^{-4}$, with a fivefold enhancement when compared with H II regions. In the warped disk model above, we expect $\phi = 3$–30×10^4 photons cm^{-2} s^{-1}. Only the high end of this range is sufficient for explaining the Hα recombination emission. For a gas disk with a thickness of 1 kpc, $\mathscr{E}_m = 0.1$ cm^{-6} pc implies $n_e \approx 0.01$ cm^{-3}, such that for a fully ionized gas, $U = 10^{-5}$ to 10^{-4}. The high end of this range is indeed where the [N II] λ6548/Hα ratio peaks in Figure 10. The observed ratio ([N II] λ6548/H$\alpha \approx 1$) implies that [N II] λ6583/Hα (≈ 3) is a factor of 2 higher than the peak of the curve in Figure 10. While this model may have some application to the H I edges of NGC 253, a full explanation of the gas excitation requires an additional heat source.

Our attempt to explain the enhanced [N II]/Hα ratios with the dilute, hardened radiation field is made much more difficult if the particle column density seen from the nucleus is much less than 3×10^{19} atoms cm^{-2}. It is noteworthy that [O I] λ6300 is produced deep within the slab, compared to [O II] and [O III]. The relative strength of these lines exhibits a complex interdependence of the shape of the ionizing spectrum, the ionization parameter, and, most crucially, the column density of the ionized gas. Figure 10 illustrates that, in fact, all emission lines exhibit some dependence on the gas column density.

Rand (1997) emphasizes the importance of the He I λ5876/Hα and the [N II]/Hα ratios, taken together, for constraining the He ionizing fraction and the ionizing spectrum. Domgörgen & Mathis (1994) predict a high He ionizing fraction if the enhanced [N II] emission results from a dilute, hardened radiation field. A direct measurement of the kinetic temperature is possible from a detection of the [N II] λ5755 line (Osterbrock 1989). But these V-band lines are expected to be an order of magnitude fainter than Hα, which puts them at the limit of detectability (BTVS).

Finally, we summarize the steps that were taken to achieve the enhanced low-ionization line ratios in Figure 10. If [N II] λ6583/H$\alpha = 0.3$ is typical for a high-U model (e.g., H II region), a dilute radiation field ($U < 0.01$) in the neighborhood of hot stars can double this ratio (e.g., Mathis 1986). Hardening the dilute radiation field with interstellar absorption can produce line ratios closer to unity (e.g., Sokolowski 1994). An additional 50% increase is achieved with the known gas-phase depletions of refractory elements. Further enhancement of this ratio (for a fixed abundance) requires that we selectively heat the electrons without producing a higher ionization state of nitrogen.

7. CONCLUSIONS

We have succeeded in detecting ionized gas at and beyond the H I cutoff radius in the nearby spiral galaxy NGC 253. This galaxy is a member of a small ensemble, the Sculptor group, with a low internal dispersion and little or no associated hot medium. The detected emission measures of the Hα and [N II] lines are sufficiently strong that it is unlikely that the source of the ionization is the metagalactic UV background. The strength of the [N II] line with respect to the Hα line argues for an enhanced electron temperature at large galactic radius, compared with the inner H II regions. The dominant ionization mechanism is suspected

to be caused by hot young stars in the inner regions that see the warped outer H I disk. We present a composite ionization model that may have some application to the H I edges of NGC 253, but a full explanation requires additional heat sources. The kinematic measurements confirm that the rotation curve is still rising at and beyond the H I edge. In some respects, since the H I disk ceases to be detectable at only $1.2R_{25}$, this is not an ideal object for testing the original proposal of Bochkarev & Sunyaev (1977). But there are a few objects that subtend a large solid angle on the sky and have H I disks extending to beyond $2R_{25}$: these will be the focus of subsequent papers.

J. B. H. wishes to thank Oxford University for a Visiting Fellowship and for hospitality during the preparation of this manuscript. We acknowledge extended dialogues with Dennis Sciama, Jon Weisheit, and James Binney. We are indebted to Walter Dehnen for his insights and for carrying out a least-squares fit to our data. Both an anonymous referee and the Scientific Editor, G. D. Bothun, made substantive comments that improved the presentation of this manuscript. Keith Taylor and Sylvain Veilleux assisted in some of the observations, and the etalon was loaned to us by Brent Tully. We acknowledge comments from George Field, communicated by Dennis Sciama. J. B. H. wishes to thank Jim Sokolowski for permission to reproduce unpublished work arising from extensive collaborations.

REFERENCES

Adams, F. C., & Laughlin, G. 1996, ApJ, 468, 586
Antonucci, R. R. J., & Ulvestad, J. S. 1988, ApJ, 330, L97
Arp, H. 1985, AJ, 90, 1012
Bahcall, J. N., et al. 1991, ApJ, 377, L5
Baldwin, J., et al. 1991, ApJ, 374, 580
Bania, T. M. & Lyon, J. G. 1980, ApJ, 239, 173
Beck, S. C., & Beckwith, S. V. 1984, MNRAS, 207, 671
Benjamin, R. A., & Shapiro, P. R. 1993, in The Evolution of Galaxies and Their Environment, ed. D. J. Hollenbach, H. A. Thronson, & J. M. Shull (NASA CP-3190) (Mottett Field, CA: NASA), 338
Bica, E., & Alloin, D. 1987, A&A, 70, 281
Bland-Hawthorn, J., Ekers, R. D., van Breugel, W., Koekemoer, A., & Taylor, K. 1995, ApJ, 447, L77
Bland-Hawthorn, J., & Maloney, P. R. 1997, ApJ, in press (BM)
Bland-Hawthorn, J., Taylor, K., Veilleux, S., & Shopbell, P. L. 1994, ApJ, 437, L95 (BTVS)
Bochkarev, N. G., & Sunyaev, R. A. 1977, Soviet Astron., 21, 542 (originally 1975, AZh, 54, 957)
Boggs, P. T., Byrd, R. H., & Schnabel, R. B. 1987, SIAM J. Sci. & Stat. Computing, 8(6), 1052
Bosma, A. 1978, Ph.D. thesis, Univ. Groningen
Bowyer, S. 1991, ARA&A, 29, 59
Carignan, C. 1985, ApJ, 299, 59
———. 1991, in Proc. Space Telescope Workshop on Dark Matter (Baltimore: STSI)
Carignan, C., & Freeman, K. C. 1985, 294, 494
Chabrier, G., Segretain, L., & Méra, D. 1996, ApJ, 468, L21
Charlot, S., & Silk, J. 1995, ApJ, 445, 124
Corbelli, E., & Salpeter, E. E. 1988, ApJ, 326, 551
Corbelli, E., Schneider, S. E., & Salpeter, E. E. 1989, AJ, 97, 390
Cowie, L. L., & Songaila, A. 1986, ARA&A, 24, 499
Cruddace, R., et al. 1974, ApJ, 187, 497
Dehnen, W., & Binney, J. 1997, MNRAS, in press
Diaz, A. I. 1989, in Evolutionary Phenomena in Galaxies, ed. J. E. Beckman & B. E. J. Pagel (Cambridge: Cambridge Univ. Press), 377
Domgörgen, H., & Mathis, J. S. 1994, ApJ, 428, 647
Dopita, M. A., & Sutherland, R. 1996, ApJS, 102, 161
Dove, J. B., & Shull, J. M. 1994, ApJ, 423, 196
Draine, B. T., & Lee, H. M. 1984, ApJ, 285, 89
Evans, N., & Dopita, M. A. 1985, ApJS, 58, 125
Fadda, D., et al. 1996, ApJ, 473, 670
Ferland, G. 1991, Cloudy Code, OSU Internal Report, 91-01
———. 1992, ApJ, 389, L63
Ferland, G., & Mushotzky, R. 1984, ApJ, 286, 42
Ferland, G., & Netzer, H. 1983, ApJ, 264, 105
Freeman, K. C. 1993, in Physics of Nearby Galaxies: Nature or Nurture, ed. Trinh Thuan et al. (Paris: Editions Frontières), 201
———. 1996, in Unsolved Problems of the Milky Way, ed. L. Blitz & P. Teuben (Dordrecht: Kluwer), 645
Grevesse,, & Anders, E. 1989, in AIP Conf. Proc. 183, Cosmic Abundances of Matter, ed. C. J. Waddington (New York: AIP), 183
Haardt, F., & Madau, P. 1996, ApJ, 461, 20
Halpern, J. P., & Steiner, J. E. 1983, ApJ, 269, L37
Haynes, M. P., & Roberts, M. S. 1979, ApJ, 227, 767
Henry, R. C. 1991, ARA&A, 29, 89
Henyey, L. G., & Greenstein, J. L. 1941, ApJ, 93, 70
Hogan, C. J., & Weymann, R. J. 1987, MNRAS, 225, 1P
Jenkins, E. B. 1987, in Interstellar Processes, ed. D. J. Hollenbach & H. A. Thronson (Dordrecht: Reidel), 533
Jura, M. 1980, ApJ, 241, 965
Kamphuis, J. 1993, Ph.D. thesis, Univ. Groningen
Kawaler, S. 1996, ApJ, 467, L61
Kondratyev, K. Ya. 1969, in Radiation in the Atmosphere (New York and London: Academic)
Koribalski, B., Whiteoak, J. B., & Houghton, S. 1995, Proc. Astron. Soc. Australia, 12, 20
Kurucz, R. L. 1979, ApJS, 40, 1
Lee, Y.-W. 1993, in ASP Conf. Ser. 48, The Globular Cluster–Galaxy Connection, ed. G. H. Smith & J. P. Brodie (San Francisco: ASP), 142
Liebert, J., Dahn, C. C., & Monet, D. G. 1988, ApJ, 332, 891
Lyon, J. G. 1975, ApJ, 201, 168
Maeder, A. 1990, A&AS, 84, 139
Malin, D. F. 1981, J. Phot. Sci., 29, 199
———. 1983, in IAU Colloq. 78, Astronomy with Schmidt-Type Telescopes, ed. M. Capaccioli (Dordrecht: Reidel), 57
Maloney, P. 1993, ApJ, 414, 41
Martin, P. G., & Rouleau, F. 1990, preprint
Mathewson, D. S., Cleary, M. N., & Murray, J. D. 1975, ApJ, 195, L97
Mathewson, D. S., & Ford, V. L. 1984, in IAU Symp. 108, Structure and Evolution of the Magellanic Clouds (Dordrecht: Reidel), 125
Mathis, J. 1986, ApJ, 301, 423
Mathis, J., Rumpl, W., & Nordsieck, K. H. 1977, ApJ, 217, 425
Mihalas, D. 1972, Non-LTE Model Atmospheres for B & O stars (NCAR-TN/STR-76)
Miller, G. E., & Scalo, J. M. 1979, ApJS, 41, 513
Molla, M., Ferrini, F., & Diaz, A. I. 1996, ApJ, 466, 668
Nordgren, T. E., Cordes, J. M., & Terzian, Y. 1992, AJ, 104, 1465
Olling, R. P. 1995, 110, 591
Osterbrock, D. E. 1989, Astrophysics of Gaseous Nebulae and Active Galactic Nuclei (Mill Valley: Univ. Sci. Books)
Osterbrock, D. E., & Martel, A. 1992, PASP, 104, 76
Pagel, B. E. J. 1989, in Evolutionary Phenomena in Galaxies, ed. J. E. Beckman & B. E. J. Pagel (Cambridge: Cambridge Univ. Press), 201
Puche, D., & Carignan, C. 1991, ApJ, 378, 487
Puche, D., Carignan, C., & van Gorkom, J. 1991, AJ, 101, 456 (PCvG)
Rand, R. 1997, ApJ, 474, 129
Raymond, J. 1990, ApJ, 365, 387
Reynolds, R. J., & Cox, D. P. 1992, ApJ, 400, L33
Rots, A. H. 1975, A&A, 45, 43
Ryder, S., et al. 1996, Proc. Astron. Soc. Australia, 14, 81
Ryu, D., Olive, K. A., & Silk, J. 1990, ApJ, 353, 81
Salpeter, E. E. 1955, ApJ, 121, 161
Salucci, P., & Frenck, C. S. 1989, MNRAS, 237, 247
Sargent, W. L. W., & Steidel, C. C. 1990, in Baryonic Dark Matter, ed. D. Lynden-Bell & G. Gilmore (Dordrecht: Kluwer), 223
Savage, B. D., & Massa, D. 1987, ApJ, 314, 380
Schommer, R. A., et al. 1993, AJ, 105, 97
Sciama, D. W. 1995, MNRAS, 276, L1
———. 1996, Modern Cosmology and the Dark Matter Problem (Cambridge: Cambridge Univ. Press)
Shields, J. C. 1992, ApJ, 339, L27
Slavin, J. D., Shull, J. M., & Begelman, M. C. 1993, ApJ, 407, 83
Smith, G. P. 1963, Bull. Astron. Inst. Netherlands, 17, 203
Sokolowski, J. 1994, preprint
Sokolowski, J., & Bland-Hawthorn, J. 1991, PASP, 103, 911
Spyromilio, J. 1995, MNRAS, 277, L59
Staveley-Smith, L., et al. 1990, ApJ, 364, 23
Sutherland, R. S., & Dopita, M. A. 1993, ApJS, 88, 253
Tarter, C. B., Tucker, W. H., & Salpeter, E. E. 1969, ApJ, 156, 943
van Albada, T. S., Bahcall, J. N., Begeman, K., & Sancisi, R. 1985, ApJ, 295, 305
van Gorkom, J. H. 1993, in The Environment and Evolution of Galaxies, ed. J. M. Shull & H. A. Thronson (Dordrecht: Kluwer), 345
Veilleux, S. 1988, Ph.D. thesis, Univ. California Santa Cruz
Vogel, S. N., Weymann, R., Rauch, M., & Hamilton, T. 1995, ApJ, 441, 162
Wakker, B. P. 1991, A&AS, 90, 495
Wood, P. 1990, JRASC, 84, 150
Yelle, R. V., & Roesler, F. 1985, J. Geophys. Res., 90, 7568
Zaritsky, D., Smith, R., Frenk, C., & White, S. D. M. 1997, ApJ, 478, 39